The Thousand-Pulsar-Array programme on MeerKAT – XIII. Timing, flux density, rotation measure, and dispersion measure time series of 597 pulsars

M. J. Keith [1]★ S. Johnston [2] A. Karastergiou,[3] P. Weltevrede [1] M. E. Lower [2] A. Basu,[1] B. Posselt [3] L. S. Oswald [3,4] A. Parthasarathy [5] A. D. Cameron,[6,7] M. Serylak[8,9] and S. Buchner[10]

[1]*Jodrell Bank Centre for Astrophysics, Department of Physics and Astronomy, University of Manchester, Manchester M13 9PL, UK*
[2]*Australia Telescope National Facility, CSIRO Space and Astronomy, PO Box 76, Epping NSW 1710, Australia*
[3]*Department of Astrophysics, University of Oxford, Denys Wilkinson Building, Keble Road, Oxford OX1 3RH, UK*
[4]*Magdalen College, University of Oxford, Oxford OX1 4AU, UK*
[5]*Max-Planck-Institut für Radioastronomie, Auf dem Hügel 69, D-53121 Bonn, Germany*
[6]*Centre for Astrophysics and Supercomputing, Swinburne University of Technology, PO Box 218, VIC 3122, Australia*
[7]*ARC Centre of Excellence for Gravitational Wave Discovery (OzGrav), Swinburne University of Technology, PO Box 218, VIC 3122, Australia*
[8]*SKA Observatory, Jodrell Bank, Lower Withington, Macclesfield, SK11 9FT, UK*
[9]*Department of Physics and Astronomy, University of the Western Cape, Bellville, Cape Town 7535, South Africa*
[10]*South African Radio Astronomy Observatory, 2 Fir Street, Black River Park, Observatory 7925, South Africa*

ABSTRACT
We report here on the timing of 597 pulsars over the last four years with the MeerKAT telescope. We provide times of arrival, pulsar ephemeris files, and per-epoch measurements of the flux density, dispersion measure (DM), and rotation measure (RM) for each pulsar. In addition, we use a Gaussian process to model the timing residuals to measure the spin frequency derivative at each epoch. We also report the detection of 11 glitches in nine individual pulsars. We find significant DM and RM variations in 87 and 76 pulsars, respectively. We find that the DM variations scale approximately linearly with DM, which is broadly in agreement with models of the ionized interstellar medium. The observed RM variations seem largely independent of DM, which may suggest that the RM variations are dominated by variations in the interstellar magnetic field on the line of sight, rather than varying electron density. We also find that normal pulsars have around 5 times greater amplitude of DM variability compared to millisecond pulsars, and surmise that this is due to the known difference in their velocity distributions.

Key words: pulsars: general – ISM: general.

1 INTRODUCTION

The radio emission from pulsars is thought to originate from close to the surface of the star and locked to its rotation. The radio emission is usually highly linearly polarized and is beamed along the magnetic axis, resulting in pulses of emission being detected by a distant observer. The time-of-arrival (ToA) of the pulses at an Earth-based observatory yields much information, it tells us the rotation rate of the pulsar, how fast it slows down, how irregular the slow-down is and about transient events such as glitches. Together, these inform us about the evolution of pulsars over time and provides insight into the composition and structure of the neutron star interior. Additionally, the traverse of the emission through the interstellar medium (ISM) gives information on the composition, structure, and magnetic fields of the ISM via measurements of dispersion measure (DM; e.g. Yao, Manchester & Wang 2017) and rotation measure (RM; e.g. Han et al. 2018).

The Thousand Pulsar Array (TPA) programme on the MeerKAT telescope (Johnston et al. 2020) forms part of the larger MeerTime key science project (Bailes et al. 2020). The top-level goals of the TPA are two-fold. First, to use the full sensitivity of the MeerKAT telescope to provide a census of both the integrated and single-pulse properties for more than 1000 pulsars (Posselt et al. 2021, 2023; Johnston et al. 2023; Song et al. 2023). The second major goal is to investigate the time-varying properties of pulsars through regular, high fidelity (Song et al. 2021) observations of a large (∼600) and diverse sample of pulsars. These observations have a median cadence of 27 d, though the exact observing pattern has changed several times over the course of the programme primarily due to scheduling constraints on the telescope.

This paper describes the data products from the TPA regular monitoring programme that are published alongside this paper. This first data release consists of ToAs and pulsar ephemerdies for 597 pulsars, as well as measurements of spin-down rate, flux density, RM, and DM for each pulsar over the period 2019 March to 2023 May. Pulse profile shapes are also monitored within the TPA, details of which will appear in a subsequent paper, with initial results published in Basu et al. (2024).

★ E-mail: Michael.Keith@manchester.ac.uk

Section 2 briefly outlines the observations and defines the sample of pulsars in the data release. Section 3 describes the methods used to measure each of the parameters presented in the tables and figures comprising the data release, which are themselves described in Section 4. Some broad highlights of the data are presented in Section 5, with a particular focus on the measurements of DM and RM variations as an example of what may be done using the data.

2 THE TPA DATA

2.1 Observations

Observations for the TPA programme fall into two categories. For the census projects, observations were carried out with at least 60 antennas of the MeerKAT array. Observations were done with the *L*-band receiver and, generally, every pulsar was observed once with an integration time determined using the prescription outlined in Song et al. (2021). For the monitoring project we aim to observe some 500 pulsars once per month. These observations split the array into two sub-arrays each consisting of ∼30 antennas. Here, observation times are very short (typically less than 2 min in duration) in order to observe as many pulsars as possible in the monthly allocation of 16 h of telescope time. The data in this data release combine both types of observations, though the vast majority of data values come from the regular observations. Although we aim for continuous observations with a regular sampling, around half of the pulsars exhibit a gap in observations due to periods where pressure on available telescope time required us to reduce the number of pulsars observed. Hence, there is a gap of around 1 yr, from 2021 March to 2022 February, for 294 pulsars, and a gap of around 200 d, from 2019 November to 2021 May, for 74 pulsars.

A description of the observing system can be found in Bailes et al. (2020) and Johnston et al. (2020). In brief, we used the observational band from 896 to 1671 MHz with 928 frequency channels. The data are folded into sub-integrations each of length 8 s for the duration of the observation and there are 1024 phase bins per pulse period. Polarization calibration follows the method outlined in Serylak et al. (2021) and flux calibration is achieved as described in Posselt et al. (2023). Data outputs are in PSRFITS format (Hotan, van Straten & Manchester 2004). In total, more than 24 000 observations have been made for the TPA programme over the 4 yr timespan.

2.2 The pulsar sample

There are in excess of 1250 pulsars observed as part of the TPA (Posselt et al. 2023; Song et al. 2023). Many of these only have a one or two census-style observations, but there are 614 pulsars that had at least 10 observations in the period from 2019 March to 2023 May. Pulsars were selected for the regular monitoring campaign based on the quality of data that could be obtained in the very short observation time, and the list was refined several times with the priority on ensuring data of good quality whilst also trying to keep a good spread of pulsars over the *P–Ṗ* diagram (see Fig. 1) The latter criteria was included to reduce selection bias when the data are used for studies of properties of the pulsar population, though we note that the TPA does not observe millisecond pulsars (MSPs) and the MeerTime programme to observe MSPs is described elsewhere (Spiewak et al. 2022). From these 614, we exclude the 7 pulsars which have binary companions (PSRs J0045−7319, J0823+0159, J1141−6545, J1302−6350, J1740−3052, J1906+0746, and J1930−1852) as these require more careful analysis and will be described elsewhere. We further exclude
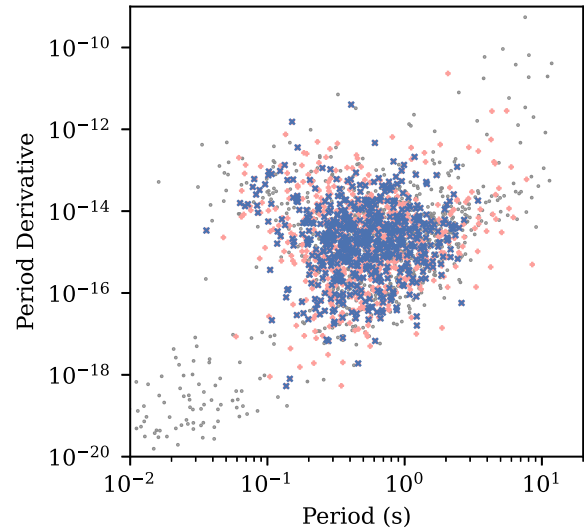

Figure 1. Period versus period derivative (*P–Ṗ* diagram) for the 597 pulsars in this data release (blue cross), the full TPA census (pink plus), and all pulsars in the ATNF pulsar catalogue (PSRCAT, version 1.70, https://www.atnf.csiro.au/research/pulsar/psrcat). Note that not all pulsars in PSRCAT are shown due to the plot axis limits.

three pulsars (PSRs J1717−4054, J1906+0414, and J1929+1357) which have a high nulling fraction and hence very few detections, and one pulsar (PSR J1644−4559) which was used mainly for system tests. Finally, there are six pulsars (PSRs J0835−4510, J1301−6305, J1420−6048, J1614−5048, J1718−3825, and J1907+0631) which we exclude as we were unable to obtain a coherent timing solution because of the presence of large glitches. There are therefore a total of 597 pulsars presented in this paper.

3 MEASUREMENT METHODOLOGY

3.1 Timing

3.1.1 Templates and ToA measurements

ToA measurements are one of the data products from the the MeerPipe pipeline which runs automatically on all TPA observations. The ToAs are computed on the eight sub-band, fully time-averaged, data using PSRCHIVE to cross correlate the observed pulse profile with a noise-free template, using the Fourier-domain Markov-chain (FDM) method in PAT (Hotan et al. 2004). A single template is used across all eight sub-bands, generated from the 'best' TPA observation, which is typically the observation from the TPA census, which uses the full MeerKAT array and much longer integration time than the typical TPA timing observations, or from averaging several observations where signal-to-noise ratio (S/N) is low. For most pulsars the noise-free template is generated by means of a Gaussian process (GP) modelling of the observed average pulse profile (Johnston & Karastergiou 2019). To improve the performance of the template, the profile is tapered off to zero outside the on-pulse window computed in Posselt et al. (2021), which ensures that no information from the off-pulse is used in the template matching. Each automated template was inspected and for 58 pulsars, notably those with scattering tails, interpulses or very complex shapes, the automated template generation was deemed unsuitable. For these

pulsars, templates were computed by fitting von Mises functions[1] 'by hand' using PAAS from PSRCHIVE, or in the case of two highly scattered pulsars (PSRs J1701−4533 and J1828−1101), using von Mises functions convolved with a single exponential with a bespoke routine. Since only a single template was used across the whole band, users should be aware that the resulting ToAs will include effects of profile evolution which must be accounted for in any later timing analysis.

Initial timing was performed using TEMPO2 to compute and fit the timing residuals. The initial ephemeris was taken from PSRCAT, and coarsely refined whilst searching for possible phase wraps between observing epochs. For some pulsars with significant spin noise or glitch activity, the catalogue ephemerides lost phase at a rate of up to several turns per day, so for some cases we relied on ephemerides provided by long-term timing programmes with the Lovell telescope at Jodrell Bank Observatory, or the Murriyang telescope at Parkes Observatory.

The MeerPipe pipeline produces ToAs from all observing epochs, even if the pulsar was not detected, or the observation was corrupted by interference. Therefore some removal of bad data is needed, and ToAs were discarded if the pulsar was not detected, or if the ToA uncertainty was so great as to not provide useful information to the timing. In most cases, the lack of detection is due to pulsars with known nulling, or weak modes that are not detectable in the typical TPA timing observations with less than 2 min durations.

3.1.2 The timing model

The final TPA timing data product was refined from the coarse timing model by means of applying a Bayesian noise modelling simultaneously with the timing model fitting. The pulse noise model consists of a time-correlated achromatic spin noise, plus a time uncorrelated white noise component. The achromatic spin noise is implemented using the Fourier-domain GP as described in Lentati et al. (2013) to model the noise by a power-law parametrized by dimensionless amplitude $A_{\rm red}$ and slope γ, and power spectral density given by

$$P(f) = \frac{A_{\rm red}^2}{12\pi^2} \left(\frac{f}{f_{\rm yr}}\right)^{-\gamma} f_{\rm yr}^{-3}, \qquad (1)$$

where $f_{\rm yr}$ is a frequency of 1 yr^{-1}. The white noise consists of the widely used EFAC and EQUAD parameters that scale and add in quadrature the independent white noise for each observation, plus an additional ECORR term correlated across observations at each epoch. For ToAs with formal error given by σ_i, the white noise covariance matrix is given by

$$\mathbf{C} = \text{EFAC}^2 \, \mathbf{\Sigma} + \text{EQUAD}^2 \, \mathbf{I} + \text{ECORR}^2 \, \mathbf{\Delta}, \qquad (2)$$

where $\mathbf{\Sigma}$ is a diagonal matrix with $\Sigma_i = \sigma_i^2$, $\mathbf{I}$ is the identity matrix, and $\mathbf{\Delta}$ is a block-diagonal matrix such that $\Delta_{i,j} = 1$ for i, j from the same observing epoch and 0 otherwise (see e.g. van Haasteren & Vallisneri 2014 for a detailed description).

In addition to fitting for the noise parameters, we also marginalize over the following parameters in the pulsar ephemeris using the linearized model of TEMPO2:

(i) F0, F1, and F2 – Spin frequency and two derivatives.

(ii) RAJ and DECJ – the position of the pulsar in J2000 coordinates.

(iii) Glitch parameters (GLF0, GLPH), if required.

(iv) DM at each observing epoch.

(v) Arbitrary phase jumps for six of eight sub-bands.

The arbitrary phase jumps between sub-bands absorb any evolution of the pulse profile with frequency. In principle, we may wish to fit for phase jumps between all eight sub-bands, however, this would be fully covariant with the 'zero phase' parameter that is always fit within TEMPO2. Additionally, although the change in DM from epoch to epoch would be well measured, the average of the DM parameters would be unconstrained and hence not produce meaningful results. Therefore, we must leave two of the sub-bands phase without a phase jump in order to define the long-term average DM, and so that the fit is not degenerate with the zero phase parameter. In practice then the 'zero phase' parameter becomes defined by the average phase of these two sub-bands, and the long-term average DM is defined by the phase difference between these two sub-bands. In this analysis, we chose to keep fixed the top and bottom sub-bands, so that the average DM is determined using the most widely separated frequency channels, i.e. those centred at approximately 944 and 1623 MHz. We note that since the phase jumps are constant in time, the choice of sub-bands to fit only affects the average DM, and not the epoch-to-epoch variability, which is the main focus of this work.

The noise modelling is performed using RUN_ENTERPRISE (Keith, Niţu & Liu 2022; Keith & Niţu 2023), which is based on the ENTERPRISE framework (Ellis et al. 2019), and sampling is performed using EMCEE (Foreman-Mackey et al. 2013). The resulting noise model is then used to fit for the maximum likelihood values for the pulsar timing parameters using TEMPO2.

3.2 Time series of the spin-down rate

The timing residuals obtained for each pulsar are used to drive a time-domain GP, following section 3.2 of Brook et al. (2016). We use the same software and process used for the recent analysis of PSR J0738 4042 by Lower et al. (2023) to obtain $\dot{\nu}$ and its associated uncertainty. The GP is constructed with a single squared exponential kernel and a white noise term, and the second derivative of the GP can be directly computed to derive $\dot{\nu}(t)$. We sampled the GP hyperparameter posterior distributions using BILBY (Ashton et al. 2019) as a wrapper for the DYNESTY nested sampling algorithm (Speagle 2020). We then generated $\dot{\nu}$ points at each observing epoch directly from the GP. As always with this analysis, the assumption is that the residuals can be entirely explained by a time-variable $\dot{\nu}$. In the majority of cases, the GP models the residuals extremely well, but there may be examples where the use of an additional kernel, together with strong priors on the hyperparameters, would result in a better fit. We also caution that the uncertainties for $\dot{\nu}$ can depend on the choice of kernel, and are only correct under the above assumptions.

3.3 Dispersion measure versus time

The DM of a pulsar measures the integral of the electron density, n_e along the line of sight, L,

$$\text{DM} = \int_0^L n_e(s) \, ds. \qquad (3)$$

Observationally, the DM can be obtained by measuring the time delay between the arrival times (t_1 and t_2) of the radio pulse at two

---

[1] Functions with the form of the unnormalized von Mises distribution, $f(\phi) = \exp(-\cos(\phi))$.

different frequencies (ν_1 and ν_2) via

$$\mathrm{DM} = K \frac{t_2 - t_1}{\nu_2^{-2} - \nu_1^{-2}}, \tag{4}$$

where K is the dispersion constant and is equal to $2.410 \times 10^{-4}\,\mathrm{MHz^{-2}\,cm^{-3}\,pc\,s^{-1}}$ (see Kulkarni 2020 for a discussion of this value). In practice the DM to a pulsar is not a constant, and we measure the DM for each epoch as part of the pulsar timing process described in Section 3.1.2. It is worth noting that although the time dependence of the DM is usually well measured, there may be a systematic error in the DM if there is significant pulse profile evolution across the band, including effects from scattering. In order to get an indication of the scale of this systematic error, we compute the change in the estimated mean DM if we reference the DM against the highest or lowest pair of sub-bands rather than the most widely spaced sub-bands. It should be noted that this systematic error shifts all DM values up or down together, and does not change the perceived time variability.

3.4 Rotation measure versus time

The RM of a pulsar measures the integral of the product of the electron density and the magnetic field parallel to the line of sight ($B_\parallel$).

$$\mathrm{RM} = \frac{e^3}{2\pi m_e^2 c^4} \int_o^L n_e(s) B_\parallel(s) \mathrm{d}s, \tag{5}$$

where m_e and e are the mass and charge of an electron, respectively. Observationally, the RM can be obtained by measuring the change in the position angle (PA) of the linearly polarized radiation at two observing wavelengths (λ_1 and λ_2).

$$\mathrm{RM} = \frac{\mathrm{PA}_2 - \mathrm{PA}_1}{\lambda_2^2 - \lambda_1^2}. \tag{6}$$

In practice, several different methods are employed to determine the RM and its error bar.

Here, the methodology as described in Ilie, Johnston & Weltevrede (2019), and implemented in PSRSALSA[2] (Weltevrede 2016) is used. It is based on the RM synthesis technique (RMST; e.g. Brentjens & de Bruyn 2005), which optimizes the degree of linear polarization as function of RM. Uncertainties are estimated via bootstrapping the data. This relies on the identification of an on- and off-pulse region, which is done automatically using the same methodology as explained in Song et al. (2023), and relies on the profile templates (see also Section 3.1.1).

The RM as measured at the telescope is determined for each epoch, resulting in a time series of RM measurements. Observations with very weak detections of the pulse profile, for instance because of radio frequency interference (RFI) , were ignored in the analysis. This was done by visually inspecting pulse profiles of the in total 24 592 observations. To make this process more efficient, the pulse profiles of each pulsar are rank-ordered by the S/N. The pulse profiles for each pulsar were visually inspected starting with the lowest S/N, and observations were rejected until a pulse profile of sufficient quality was encountered. Higher S/N detections were accepted without further visual inspection. In total, 703 observations out of a total of 24 592 are excluded from the RM time series in this way.

The Earth's ionosphere contributes to the value of RM and this varies with time. This contribution was predicted using the IONFR package[3] (Sotomayor-Beltran et al. 2013), which relies on global Total Electron Content (TEC) values.[4] The predicted ionospheric contribution to the RM is subtracted in the figures (such as Fig. 7, and the figures in the data release). In the tables of the data release the measured RM (which includes a contribution of the ionosphere) and the predicted RM contribution by the ionosphere are reported separately for each observation.

3.5 Flux density

Flux calibration is carried out following the procedure described in Posselt et al. (2023). In brief, the flux densities are scaled from the system counts via the radiometer equation and by using observations of pulsars at high Galactic latitude (where the sky temperature is well-understood) to calibrate the the sky temperatures of all other pulsars. The scatter in the observed flux density is generally much larger than the formal uncertainty. Intrinsically, the flux density of a pulsar is observed to be largely stable with a low modulation index (see e.g. Kumamoto et al. 2021). However, this is only true for observations of long duration (several thousand pulse rotations). In the monitoring programme, a pulsar is typically observed for only 90 s or a few hundred rotations at best. The measured flux density will then fluctuate about some mean, depending on the random selection of single pulse flux densities from the underlying (and unknown) distribution. Furthermore, the traverse of the radio emission through the turbulent interstellar medium causes diffractive and refractive scintillation, which manifests itself as frequency and time dependent flux density variations. If these variations have comparable bandwidth and time-scales to the observations, high modulation will be seen in the light curves (Kumamoto et al. 2021). Finally, pulsars are observed to have a steep spectral index (Jankowski et al. 2018; Swainston et al. 2022; Posselt et al. 2023) and averaging in frequency over a large bandwidth biases the flux densities towards lower frequencies than the nominal centre of the band.

With all these caveats in mind, here, we simply average the pulse profile data in time and frequency for a given observation and present a single flux density for that observation.

4 DESCRIPTION OF TABLES AND FIGURES

The data described in this section can be obtained from Zenodo, doi.org/10.5281/zenodo.8430591.

4.1 Timing files

Pulsar rotational ephemerides and ToAs are provided in TEMPO2 compatible 'par' and 'tim' files. The ToAs in the tim files are annotated with a number of flags from the MeerPipe reduction pipeline, including signal-to-noise ratio (-snr) and observing time span (-length). Each ToA is also associated with a relative pulse number to enable phase tracking in TEMPO2. Each pulsar is supplied with a pair of par files. The first par file contains the complete output of the noise modelling, as produced by the Bayesian pipeline. We also provide a simplified par file without the noise modelling and

[2]https://github.com/weltevrede/psrsalsa

[3]https://github.com/csobey/ionFR
[4]We used the TEC data products provided by JPL and distributed via https://cddis.nasa.gov/archive/gps/products/ionex/.

Table 1. Description of the columns in the observation tables. Header lines give the file extension for each table. Epochs are topocentric values close to the midpoint of the observation.

Column Label	Description
	.restable
MJD	Epoch of observation
Res	Residual (s)
Res_err	Error on Residual (s)
	.dmtable
MJD	Epoch of observation
DM	Dispersion measure (cm^{-3}pc)
DM_err	Error on DM (cm^{-3}pc)
	.rmtable
MJD	Epoch of observation
RM	Rotation measure, as measured ($rad\,m^{-2}$)
RM_err	Error on RM ($rad\,m^{-2}$)
RMiono	Ionospheric Rotation Measure ($rad\,m^{-2}$)
RMiono_err	Error on Ionospheric RM ($rad\,m^{-2}$)
	.f1table
MJD	Epoch of observation
F1	GP predicted $\dot{\nu}$ (s^{-2})
F1_upperr	2σ upper error on $\dot{\nu}$ (s^{-2})
F1_lowerr	2σ lower error on $\dot{\nu}$ (s^{-2})
	.fluxtable
MJD	Epoch of observation
Flux	Phase Averaged Flux Density (mJy)
Flux_err	Error on Flux Density (mJy)

DM measurements specific to our data that is more easily transferred to other software and/or combined with data from other telescopes.

4.2 Observation tables

We provide a table containing the list of 597 pulsars we are monitoring, along with the MJD of the first and last observation and the number of data points. This table also includes the mean DM as well as the systematic offset when using either the two highest bands or the two lowest bands to define the DM. For each pulsar, in addition to the par and tim files described above, we also supply six ASCII tables, one each for the residuals, DM, RM, the rotation frequency derivative ($\dot{\nu}$), and flux density versus observation epoch. Each file has a one-line header with column labels that are described in Table 1. Measurements that are obviously spurious have been removed where, for instance, visual inspection of the observed profile suggested that the pulsar was not detected with a sufficient S/N to make a measurement of a particular parameter. Hence, the number of rows in each table may differ due to the different sensitivity to each measured parameter.

4.3 Figures

For each pulsar, we provide a visual representation of the data described above. An example plot is given in Fig. 2 for PSR J1117−6154. The five panels show the timing residual (see Section 3.1), the $\dot{\nu}$ (see Section 3.2), the DM (see Section 3.3), the RM (see Section 3.4), and the flux density (see Section 3.5) as a function of MJD. 1σ errors are shown on all values.

5 DATA HIGHLIGHTS

5.1 The interstellar medium

The strength of turbulence in the ISM can be characterized by a power law over many orders of magnitude bounded by the inner and outer scales (Rickett, Coles & Bourgois 1984). The various scales can be explored by scintillation observations (both diffractive and refractive), DM variations with time, and RM variations with time. Given dense samples and a long time-baseline, the structure function is the implement of choice for exploring the nature of the turbulence (e.g. Cordes & Rickett 1998). However, the structure function is the average power as a function of lag, and requires being able to derive multiple independent samples of the process (at the lag of interest) from the data. For most pulsars in our sample, we are only sensitive to power on the time-scale of our data set, and hence the structure functions contains little meaningful data. We therefore resort to simply measuring any gradient in the DM versus time data, which gives an indication of the strength of the DM variations on the longest time-scales. Table A1 records those pulsars for which we measure a gradient greater than 3σ from zero. There are 87 pulsars with a significant gradient (out of 597), a significantly larger fraction than the 4 out of 160 pulsars reported in Petroff et al. (2013), highlighting the improved sensitivity in the TPA data.

One also expects that the RM should change with time, particularly if the DM is also changing. In addition, however, changes in the average magnetic field strength along the line of sight should also be observed, particularly if the pulsar is in or behind a magnetic structure such as a supernova remnant. In Table A2, we list those pulsars for which the slope of RM versus time is more than 3σ significant. There are 58 such pulsars of which 15 are in common with pulsars with a DM gradient.

There are two pulsars which show very large changes in both DM and RM as shown in Fig. 3. PSR J1114−6100 has a very large RM for its location and was discussed extensively in Johnston et al. (2021). Over the course of the monitoring campaign its RM has changed by some 6 rad m^{-2} and its DM by 1 cm^{-3} pc. PSR J1833−0827 had a large negative DM slope in Petroff et al. (2013). Here, we see that the DM slope is positive and that the RM has changed by 15 rad m^{-2} in less than 2 yr. As Petroff et al. (2013) pointed out, this pulsar has an associated X-ray pulsar wind nebula (Esposito et al. 2011), making the nebula the most likely source of the fluctuations in RM and DM.

5.1.1 DM slopes versus DM

If the DM slopes we observe in our sample originate in discrete structures in the ionized ISM (IISM) then we may expect that the amplitude would scale with the square-root of the number of such structures encountered, and hence roughly with the square-root of the DM. Alternatively, we may expect that the observed DM slopes come from power on the longest length-scales in the turbulent IISM, which are expected to be at least 100 pc (Armstrong, Cordes & Rickett 1981), far longer than the scales probed by our ∼4 yr data set. To get a feeling for how the DM variations due to IISM turbulence may be expected to scale with DM, we can look at scattering, which is another effect of IISM turbulence. The 'level of turbulence' in the IISM can be estimated from measurements of interstellar scattering (Cordes 1986), where the scattering measure (SM) is the path-integrated variance in the electron density along the line of sight (Backer et al. 1993). The SM can be estimated from observations of scattering
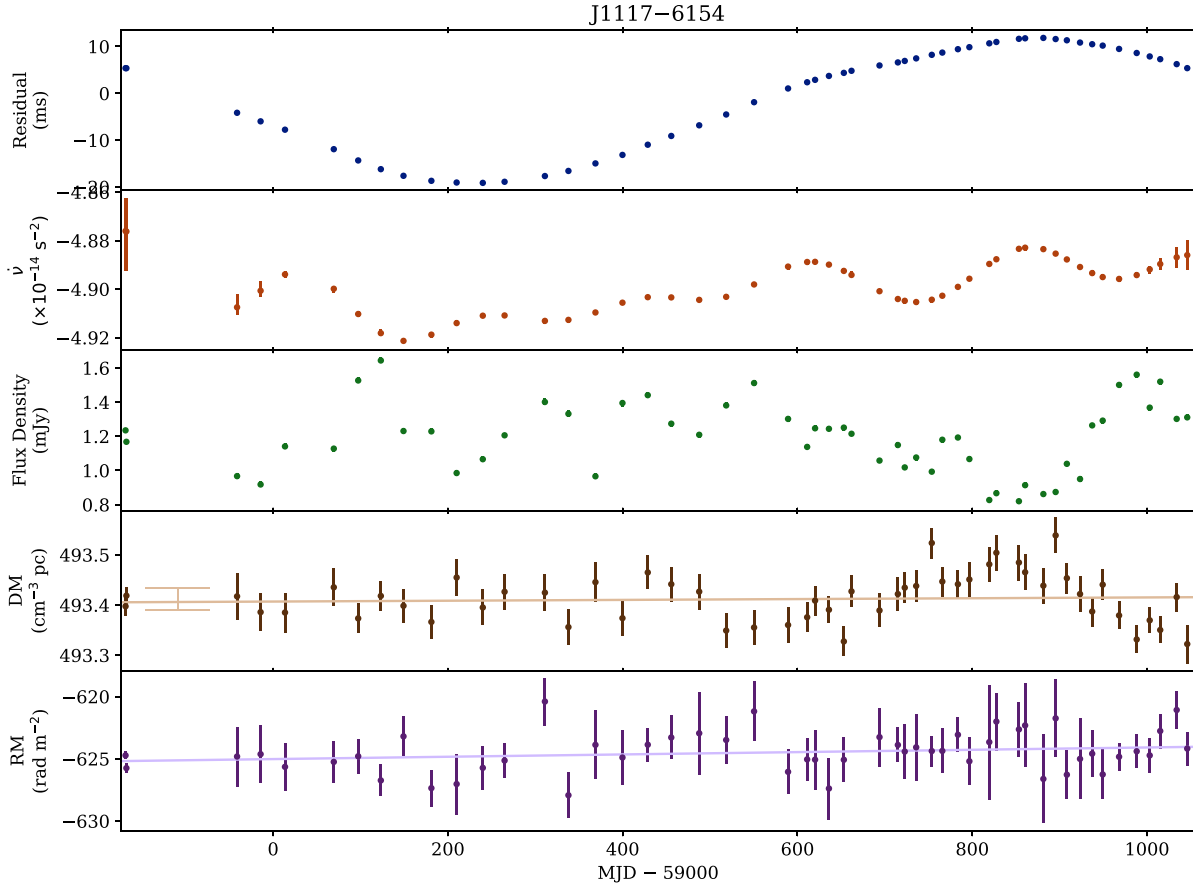
Figure 2. Top panel shows the timing residuals as a function of epoch for PSR PSR J1117−6154, followed by the values of $\dot{\nu}$, the flux density, the DM, and ionosphere corrected RM. The solid lines show the best-fitting slopes to the DM and RM versus time. 1σ errors are shown on all panels, but too small to be visible on residual and flux density. The large error bar on the DM fit represents an estimate of the systematic error in the mean DM due to frequency evolution of the pulse profile (see Section 3.3 for a description of how this is estimated).
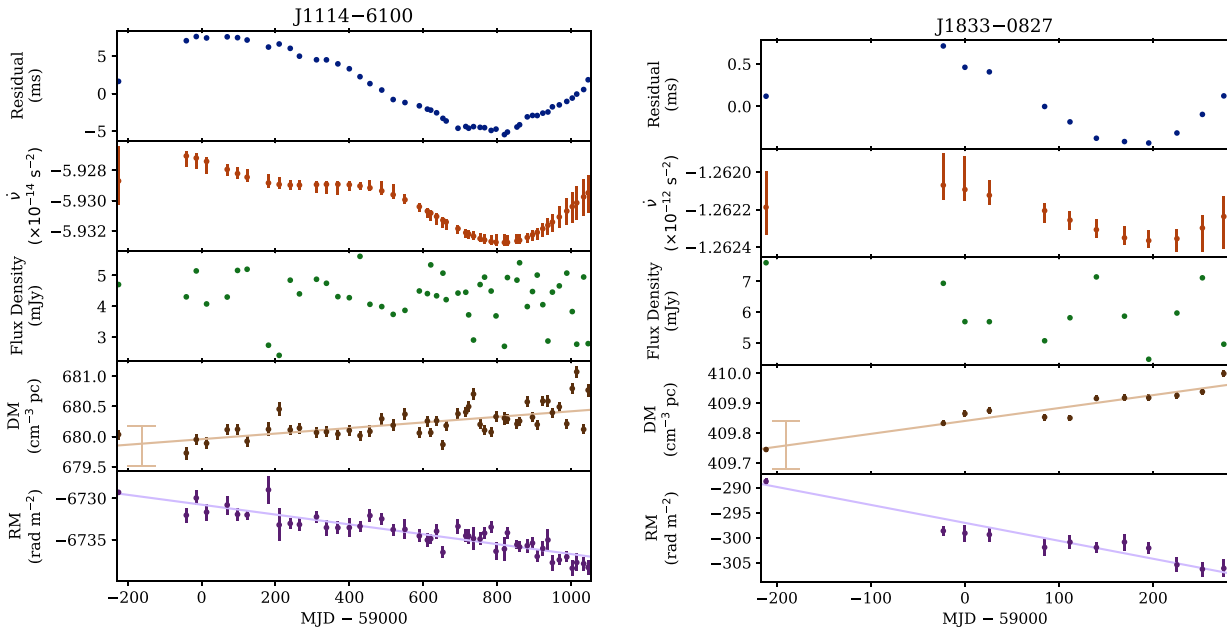

Figure 3. As Fig. 2, but for PSRs J1114−6100 (left) and J1833−0827 (right), two pulsars with significant RM and DM variations.
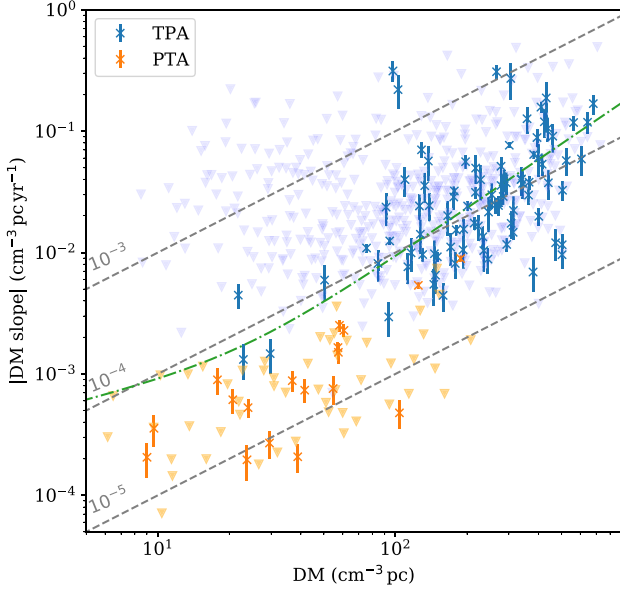
Figure 4. DM slope as a function of DM for the MeerTime TPA pulsars, and the MSPs in the MeerTime PTA data release. Downward triangles mark 2σ upper limits. Diagonal dashed lines of proportionality are shown for reference. The dot–dashed curved line shows the proportionality relationship derived from scattering measurements from equation (9).

time-scale, τ_{scatt}, where for Kolmogorov turbulence,

$$\text{SM} \propto (\tau_{\text{scatt}}/D)^{5/6}, \tag{7}$$

where D is the distance to the pulsar (Cordes et al. 1991). If the power in the IISM is independent of location then one expects to find $\tau_{\text{scatt}} \propto \text{DM}^{2.2}$, however measurements of τ_{scatt} show evidence for inhomogenities in the level of turbulence, with Krishnakumar et al. (2015) finding

$$\tau_{\text{scatt}} \propto \text{DM}^{2.2} \left(1 + 1.94 \times 10^{-3} \text{DM}^2\right), \tag{8}$$

over a the full range of DM values observed in the pulsar population.

Whilst the SM is a measure of the variance of the electron density, the amplitude of the DM variations should scale with the standard deviation of the DM, and hence all else being equal, the typical amplitude of DM slope to a pulsar should scale with the square-root of the expected SM (Backer et al. 1993). Hence, we can insert equation (8) into equation (7) and square-root. Making also the simplifying assumption that $D \propto \text{DM}$ we can get a scaling relation

$$|\text{DM slope}| \propto \text{DM}^{1/2} \left(1 + 1.94 \times 10^{-3} \text{DM}^2\right)^{5/12}. \tag{9}$$

Hence, we may expect that the exponent of DM slope to evolve slightly with DM, from 1/2 at low DM, to 4/3 at high DM, but in practice the intrinsic scatter means that this does not seem distinguishable from a DM slope linearly proportional to DM over the TPA sample.

Indeed, we find that the measured DM gradient for the TPA pulsars appears consistent with linear increase with DM with a slope of the order of $10^{-4} \times \text{DM yr}^{-1}$. Fig. 4 shows this for the TPA pulsars, and also for the sample of MSPs from the MeerTime PTA data release (Miles et al. 2023) which is much more sensitive to DM variations due to the nature of precision MSP timing. Although both seem to scale with DM, the TPA sample shows a factor of around 5 times larger DM slopes for a given DM. PTA pulsars are, due to selection effects in the discovery of pulsars, more likely to be at lower DM
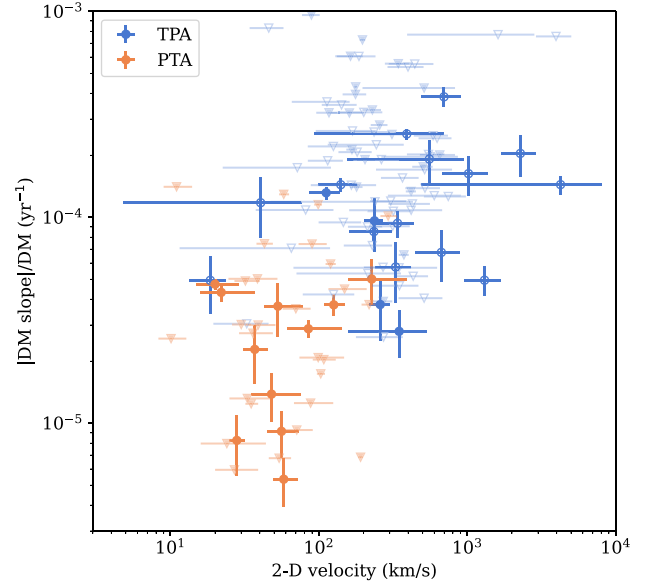

Figure 5. DM slope, scaled by DM, as a function of velocity. For TPA pulsars velocity is inferred from proper motion measurements and distance estimates taken from PSRCAT. PTA velocities taken from Shamohammadi et al. (2024). Not all pulsars have proper motions measured. Downward triangles mark 2σ upper limits. Pulsars with parallax derived distances are shown with filled symbols, those with DM-derived distances are shown with open symbols.

than the TPA sample, and hence some of the observed difference may be due to the inhomogenties in the IISM such as those which give rise to equation (9). However, as seen in the dot–dashed line in Fig. 4, the increased DM variation at large DM does not seem strong enough to explain the difference.

An important consideration for interpreting these results is that the rate at which we observe DM fluctuations does not only depend on the scale of the turbulence in the IISM, but also on the rate at which the line of sight to the pulsar traverses the IISM. For most pulsars, the line-of-sight velocity is dominated by the velocity of the pulsar, therefore, we may suppose that the the difference in scale of DM gradients may instead be due to the smaller velocity distribution observed in MSPs compared to the general pulsar population (Hobbs et al. 2005; Shamohammadi et al. 2024). Fig. 5 shows the fractional DM slope as a function of an estimate of the pulsar 2D velocity. For the PTA pulsar sample, the velocities are taken from (Shamohammadi et al. 2024), which are based on Very Long Baseline Interferometry (VLBI) or timing parallax and proper motions. This velocity for TPA pulsars is estimated from proper motion and distance as recorded in PSRCAT. Parallax measurements are used if available, or otherwise distance is inferred from the DM using the 'YMW16' electron density model (Yao et al. 2017). It should be noted that the uncertainties in the velocity of TPA pulsars are not rigorous as distance estimates can be unreliable, and we have made an assumption of normally distributed independent uncertainties on all measurements. We refer readers to Verbunt, Igoshev & Cator (2017) or Shamohammadi et al. (2024) for a complete and careful study of the intrinsic distribution of pulsar velocities. Nevertheless, studies of pulsar velocities seem clear that the 'normal' pulsar population sampled by the TPA has an average velocity at least 3 times greater than the PTA sample, and there is evidence that a large fraction of the normal pulsars have velocities 5–10 times greater (Verbunt et al. 2017; Shamohammadi et al. 2024). Therefore we feel that that the larger DM variations observed in the
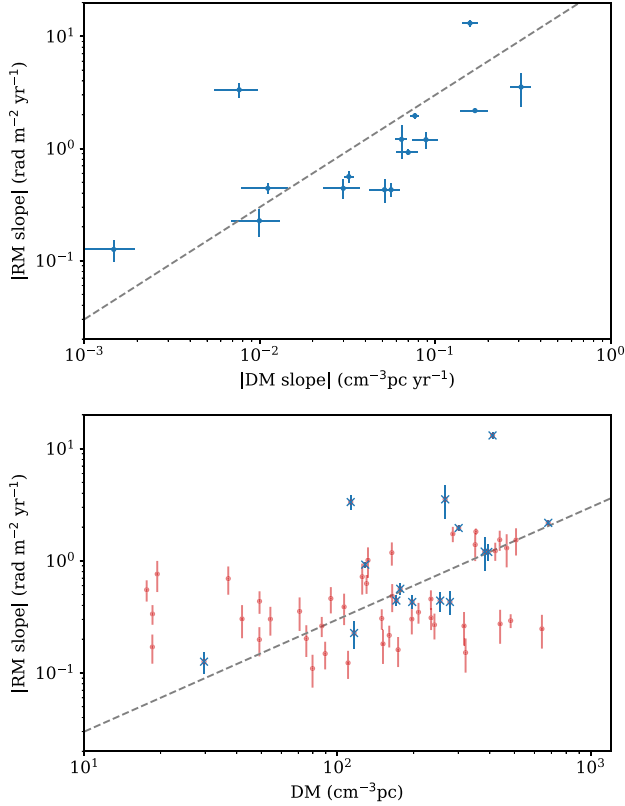
Figure 6. *Upper panel*: Magnitude of RM slope versus DM slope for the 15 pulsars where we measure both RM and DM slopes. *Lower panel*: Magnitude of RM slope versus DM for all pulsars where RM slopes were detected (red points) and those with both RM and DM slopes (blue crosses). In both panels the black grey dashed line is a line of linear proportionality.

TPA pulsars can be reasonably attributed to the fact that the line of sight to the pulsar traverses the ISM at a rate up to an order of magnitude faster than for the PTA sample. If one assumes that the observed DM slope scales linearly with pulsar velocity, and that the dependence on DM is also close to linear over the typical pulsar distance, we suggest a 'rule of thumb' for predicting the magnitude of DM variations in a pulsar by

$$|\mathrm{DM\,slope}| \sim 0.01 \,\mathrm{cm}^{-3}\,\mathrm{pc}\,\mathrm{yr}^{-1} \left(\frac{\mathrm{DM}}{100\,\mathrm{cm}^{-3}\,\mathrm{pc}} \right) \left(\frac{v}{300\,\mathrm{km\,s}^{-1}} \right),$$

$$(10)$$

where v is the pulsar's velocity. We note that in reality there are large, and potentially systematic variations in this value due to the complex structure of the IISM.

5.1.2 RM slopes versus DM

There are 15 pulsars for which we measure a significant DM slope and a significant RM slope. These are plotted in the upper panel of Fig. 6. There is a clear correlation between the magnitude of the RM and DM slopes in these pulsars. There does not appear to be any correlation between the sign of the DM slope and the relative sign of the RM slope (i.e. if the magnitude of RM is increasing or decreasing) amongst these pulsars. Put together, this suggests that for these pulsars at least, the DM slopes and RM slopes are likely arising from electron density variations in the same structures in the IISM, though these structures do not dominate the overall RM.

Table 2. Preliminary parameters for glitches for the pulsars in the sample. Note that there is only one ToA prior to the glitch in PSR J1826−1334, hence the glitch parameters are estimated by reference to pre-glitch observations from Jodrell Bank Observatory.

JNAME	Epoch (MJD)	$\Delta\nu/\nu$ ($\times 10^{-9}$)	
J1019−5749	59 182	8.3	±1.0
J1019−5749	59 265	398.3	±2.5
J1341−6023	59 450	5774.98	±0.24
J1453−6413	59 015	1.14	±0.13
J1524−5625	59 297	2076	±6
J1803−2137	58 920	4702	±11
J1826−1334	58 879	2470	±10
J1836−1008	58 950	32.8	±0.9
J1837−0604	59 610	3290	±50
J1935+2025	59 178	93	±6
J1935+2025	59 591	2840	±40

The lower panel of Fig. 6 also shows that more broadly across the TPA sample, the amplitude of the RM gradients do not scale strongly with DM, perhaps closer to $\sqrt{\mathrm{DM}}$ or even flat, rather than the linear growth seen in the DM gradients. A scaling with $\sqrt{\mathrm{DM}}$ may suggest that the RM slopes originate from a sum over discrete structures in the ISM, perhaps dominated by variations in the local magnetic fields which would be transparent to the DM. A sum over discrete structures could be expected to increase as the square root of the number of structures on the line of sight, and hence roughly as $\sqrt{\mathrm{DM}}$ (Backer et al. 1993). Hence, the observed RM slopes may have two origins, those that arise from the same turbulent IISM effects that cause the DM slopes, and hence scale proportionally with the DM slopes, and those that are caused by discrete magnetized structures on the line of sight and hence scale most closely with the square-root of the distance to the pulsar.

5.2 Glitches

Table 2 shows the preliminary results for the glitches in the sample as the fractional change in the spin frequency $\Delta\nu/\nu$ and its error. There are 11 glitches in 9 pulsars. Further studies are ongoing to fully characterize these glitches in terms of transient events or changes in $\dot{\nu}$.

Glitches of comparable size to those listed here have previously been seen in seven of the pulsars (see compilations in Lower et al. 2021 and Basu et al. 2022). For two of the pulsars we have detected glitches for the first time. PSR J1341−6023 is a canonical middle-aged pulsar; these pulsars undergo large but rare glitches. In contrast, PSR J1935+2025 has spin parameters similar to the 'Vela-like' pulsars, which undergo quasi-periodic glitches on time-scales of years to decades. In our 3 yr of monitoring this pulsar we have detected two glitches, one relatively small in amplitude and the other relatively large. Again, this behaviour is common to the Vela-like pulsars.

5.3 Variations in $\dot{\nu}$

The observed $\dot{\nu}$ variations can be broadly classified into five classes: (i) time series that show a constant slope in $\dot{\nu}$, i.e. where there is a significant $\ddot{\nu}$; (ii) constant time series with no $\dot{\nu}$ variations; (iii) time series characterized by smooth, long time-scale variations; (iv) time series that show significant short term variability; and (v) time series that show a periodic or quasi-periodic signature.
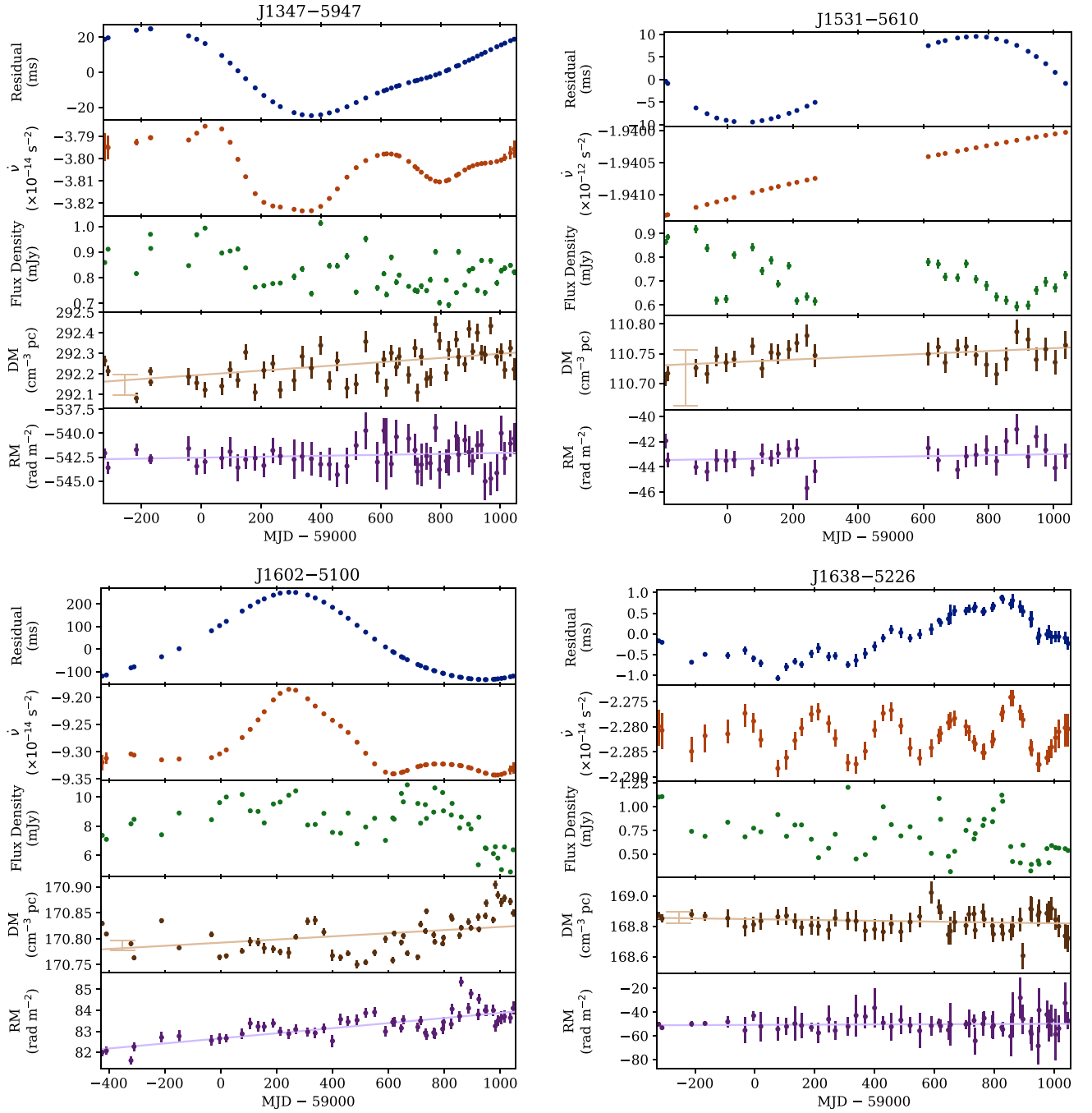
Figure 7. As Fig. 2, but for PSRs J1347−5947 (top left), J1531−5610 (top right), J1602−5100 (bottom left), and J1638−5226 (bottom right), pulsars with notable $\dot{\nu}$ variations.

Four examples of $\dot{\nu}(t)$ behaviour are shown in Fig. 7. PSR J1347−5947 shows a low level stochastic wandering of $\dot{\nu}$, seemingly typical behaviour for this type of moderate $\dot{E}$ pulsars. PSR J1531−5610 shows a straight line in $\dot{\nu}$, indicative of a large value of $\ddot{\nu}$. Indeed, $\ddot{\nu}$ was measured for this pulsar by Parthasarathy et al. (2020) who obtained a value of $1.37(2) \times 10^{-23}$ s^{-3}. The value we measure here, $1.23(5) \times 10^{-23}$ s^{-3} over a much shorter time-span is similar to their value. PSR J1602−5100 was shown by Brook et al. (2016) to undergo a profile change accompanied by a step change in $\dot{\nu}$ around MJD 54700. In the MeerKAT data, we see a similar $\dot{\nu}$ event around MJD 59 200 which also lasts for several hundred days.

Unlike the event in Brook et al. (2016), here the $\dot{\nu}$ returns to its original pre-event value. PSR J1638−5226 is an example of a pulsar with highly regular quasi-periodic oscillations in $\dot{\nu}$ with a time-scale of some 220 d. Such quasi-periodic behaviour is seen widely across the pulsar population (Hobbs, Lyne & Kramer 2010; Niţu et al. 2022) and thought to be linked to emission changes (Lyne et al. 2010).

6 CONCLUSIONS

This paper presents the first data release from the MeerTime TPA, and we highlight a few of the most striking features from the 597 pulsars.

A range of spin-down behaviours is observed, and future work will attempt to identify correlations with profile shape changes (or other properties). We also observe significant DM and RM variations in 15 per cent and 13 per cent of the pulsars over the 4 yr time-scale of our observations. These DM variations seem larger than a similar sample of MSPs, and we attribute this mainly to the different velocity dispersion in these two families of pulsars, as the line of sight traverses the ISM more quickly in the normal pulsar population. A full analysis of all the data in this data release is outside the scope of this data release paper, but we anticipate that the data will be used for a wide range of projects within the TPA and externally.

ACKNOWLEDGEMENTS

DATA AVAILABILITY

The data tables and figures in the TPA data release are available at doi.org/10.5281/zenodo.8430591. Profile data, ToAs, and other automatically produced data products can be obtained from the MeerTime Portal (https://pulsars.org.au). We request that authors cite this paper and include the zenodo DOI when making use of the TPA data release in future publications.

REFERENCES

Armstrong J. W., Cordes J. M., Rickett B. J., 1981, Nature, 291, 561
Ashton G. et al., 2019, ApJS, 241, 27
Backer D. C., Hama S., van Hook S., Foster R. S., 1993, ApJ, 404, 636
Bailes M. et al., 2020, PASA, 37, e028
Basu A. et al., 2022, MNRAS, 510, 4049
Basu A. et al., 2024, MNRAS, 528, 7458
Brentjens M. A., de Bruyn A. G., 2005, A&A, 441, 1217
Brook P. R., Karastergiou A., Johnston S., Kerr M., Shannon R. M., Roberts S. J., 2016, MNRAS, 456, 1374
Cordes J. M., 1986, ApJ, 311, 183
Cordes J. M., Rickett B. J., 1998, ApJ, 507, 846
Cordes J. M., Weisberg J. M., Frail D. A., Spangler S. R., Ryan M., 1991, Nature, 354, 121
Ellis J. A., Vallisneri M., Taylor S. R., Baker P. T., 2019, Astrophysics Source Code Library, record ascl:1912.015
Esposito P. et al., 2011, MNRAS, 416, 205
Foreman-Mackey D., Hogg D. W., Lang D., Goodman J., 2013, PASP, 125, 306
Han J. L., Manchester R. N., van Straten W., Demorest P., 2018, ApJS, 234, 11
Hobbs G., Lorimer D. R., Lyne A. G., Kramer M., 2005, MNRAS, 360, 974
Hobbs G., Lyne A. G., Kramer M., 2010, MNRAS, 402, 1027
Hotan A. W., van Straten W., Manchester R. N., 2004, PASA, 21, 302
Ilie C. D., Johnston S., Weltevrede P., 2019, MNRAS, 483, 2778
Jankowski F., van Straten W., Keane E. F., Bailes M., Barr E. D., Johnston S., Kerr M., 2018, MNRAS, 473, 4436
Johnston S. et al., 2020, MNRAS, 493, 3608
Johnston S. et al., 2021, MNRAS, 502, 1253
Johnston S., Karastergiou A., 2019, MNRAS, 485, 640
Johnston S., Kramer M., Karastergiou A., Keith M. J., Oswald L. S., Parthasarathy A., Weltevrede P., 2023, MNRAS, 520, 4801
Keith M. J., Niţu I. C., 2023, MNRAS, 523, 4603
Keith M. J., Niţu I. C., Liu Y., 2022, run_enterprise, Zenodo, doi:10.5281/zenodo.5914350
Krishnakumar M. A., Mitra D., Naidu A., Joshi B. C., Manoharan P. K., 2015, ApJ, 804, 23
Kulkarni S. R., 2020, preprint (arXiv:2007.02886)
Kumamoto H. et al., 2021, MNRAS, 501, 4490
Lentati L., Alexander P., Hobson M. P., Taylor S., Gair J., Balan S. T., van Haasteren R., 2013, Phys. Rev. D, 87, 104021
Lower M. E. et al., 2021, MNRAS, 508, 3251
Lower M. E. et al., 2023, MNRAS, 524, 5904
Lyne A., Hobbs G., Kramer M., Stairs I., Stappers B., 2010, Science, 329, 408
Miles M. T. et al., 2023, MNRAS, 519, 3976
Niţu I. C., Keith M. J., Stappers B. W., Lyne A. G., Mickaliger M. B., 2022, MNRAS, 512, 2446
Parthasarathy A. et al., 2020, MNRAS, 494, 2012
Petroff E., Keith M. J., Johnston S., van Straten W., Shannon R. M., 2013, MNRAS, 435, 1610
Posselt B. et al., 2021, MNRAS, 508, 4249
Posselt B. et al., 2023, MNRAS, 520, 4582
Rickett B. J., Coles W. A., Bourgois G., 1984, A&A, 134, 390
Serylak M. et al., 2021, MNRAS, 505, 4483
Shamohammadi M. et al., 2024, MNRAS
Song X. et al., 2021, MNRAS, 505, 4456
Song X. et al., 2023, MNRAS, 520, 4562
Sotomayor-Beltran C. et al., 2013, A&A, 552, A58
Speagle J. S., 2020, MNRAS, 493, 3132
Spiewak R. et al., 2022, PASA, 39, e027
Swainston N. A., Lee C. P., McSweeney S. J., Bhat N. D. R., 2022, PASA, 39, e056
van Haasteren R., Vallisneri M., 2014, Phys. Rev. D, 90, 104012
Verbunt F., Igoshev A., Cator E., 2017, A&A, 608, A57
Weltevrede P., 2016, A&A, 590, A109
Yao J. M., Manchester R. N., Wang N., 2017, ApJ, 835, 29

APPENDIX A: TABLES OF RM AND DM VARIATIONS

Table A1. Pulsars for which the measured slope in DM is more than 3σ away from zero. Reduced χ^2 of the linear fit is also given as an indication of the goodness of fit.

PSR	DM slope (10^{-3}cm^{-3}pc yr^{-1})		χ^2	PSR	DM slope (10^{-3}cm^{-3}pc yr^{-1})		χ^2	PSR	DM slope (10^{-3}cm^{-3}pc yr^{-1})		χ^2
J0134−2937	− 4.5	±1.0	0.22	J0807−5421	20.1	±6.4	1.3	J0849−6322	23.7	±7.2	0.96
J0904−4246	− 9.8	±2.7	1.0	J0908−4913	− 15.4	±1.5	97	J1013−5934	6.9	±2.2	3.2
J1015−5719	51.4	±9.5	1.0	J1016−5857	− 89	±15	1.2	J1019−5749	486	±70	0.23
J1042−5521	− 17.4	±4.4	2.9	J1047−6709	9.9	±3.1	15	J1048−5832	− 70	±10	13
J1057−5226	1.47	±0.46	2.0	J1105−6107	24.4	±4.4	14	J1114−6100	169	±31	5.1
J1123−4844	2.95	±0.94	1.5	J1123−6259	16.5	±4.0	0.36	J1306−6617	− 105	±23	1.1
J1326−6408	9.6	±2.3	1.6	J1341−6023	− 38.0	±4.7	2.2	J1347−5947	37.6	±7.8	3.8
J1359−6038	11.7	±1.5	44	J1412−6111	22.2	±6.7	0.65	J1507−6640	− 9.6	±1.2	2.1
J1534−4428	57	±18	0.55	J1539−5626	28.7	±6.3	0.50	J1546−5302	− 40.5	±7.5	0.91
J1550−5242	− 40	±11	0.75	J1600−5044	− 24.6	±3.6	25	J1602−5100	11.1	±3.3	31
J1609−4616	9.22	±0.74	0.62	J1611−5209	− 14.1	±4.4	1.3	J1632−4621	118	±16	2.2
J1633−5015	− 60	±18	4.0	J1637−4553	− 15.6	±3.0	1.4	J1649−3805	17.5	±2.1	0.44
J1656−3621	− 40	±13	1.2	J1658−4958	− 10.5	±3.1	0.84	J1705−1906	1.32	±0.43	0.88
J1709−4429	10.89	±0.85	3.1	J1722−3207	24.2	±5.7	1.3	J1723−3659	− 29.9	±7.1	1.1
J1739−2903	24.3	±6.3	2.3	J1744−5337	− 40	±11	0.49	J1752−2806	5.9	±1.9	20
J1759−2205	− 32.1	±2.0	20	J1807−2715	− 14.7	±2.0	2.0	J1808−3249	− 6.5	±1.9	1.6
J1809−1917	− 56.0	±7.2	1.6	J1809−2109	− 64.2	±4.7	1.6	J1813−2113	91	±24	1.0
J1816−1729	− 57	±15	1.1	J1820−0427	− 8.1	±2.3	8.2	J1828−0611	− 29.7	±5.2	1.2
J1828−1101	59	±16	1.3	J1829−1751	− 31.3	±3.3	30	J1830−0131	313	±60	0.24
J1831−0823	− 21.6	±6.9	1.3	J1832−0827	76.6	±4.3	0.68	J1833−0827	158	±16	5.1
J1834−1202	− 37.1	±9.6	0.51	J1835−1106	35.5	±9.8	2.5	J1842+1332	− 220	±67	0.75
J1843−0806	50	±13	1.6	J1845−0635	− 53	±11	1.4	J1852−0127	− 188	±62	0.96
J1857+0212	32.6	±6.1	1.9	J1901+0331	19.9	±3.3	5.3	J1902+0615	11.6	±2.7	2.4
J1903+0135	8.8	±2.1	9.0	J1904+0004	− 13.5	±2.8	2.7	J1904+0738	36	±12	0.75
J1904+0800	− 38	±10	0.59	J1906+0641	12.0	±3.5	0.72	J1906+0912	309	±41	0.50
J1908+0500	24.1	±2.2	5.0	J1909+0007	− 7.6	±2.1	1.4	J1909+0912	119	±31	1.5
J1910+0517	272	±90	1.2	J1910+0728	− 29.0	±4.3	1.9	J1913+1011	− 8.1	±2.0	0.91
J1913+1145	− 118	±24	1.3	J1913+1400	− 5.5	±1.8	0.68	J191+0219	10.4	±3.4	1.3
J1915+0838	− 126	±32	1.6	J1916+0844	40.4	±8.8	1.0	J1917+1353	12.46	±0.86	3.0

Table A2. Pulsars for which the measured slope in RM is more than 3σ away from zero. Reduced χ^2 of the linear fit is also given as an indication of the goodness of fit.

PSR	RM slope (rad m^{-2}yr^{-1})		χ^2	PSR	RM slope (rad m^{-2}yr^{-1})		χ^2	PSR	RM slope (rad m^{-2}yr^{-1})		χ^2
J0536−7543	0.336	±0.067	2.8	J0624−0424	− 0.35	±0.12	4.0	J0627+0649	− 0.262	±0.053	3.2
J0646+0905	− 0.306	±0.063	2.2	J0904−7459	0.435	±0.099	2.0	J0909−7212	0.302	±0.087	2.8
J0942−5657	0.216	±0.048	1.4	J0943+1631	− 0.76	±0.24	3.2	J1001−5507	0.63	±0.12	11
J1015−5719	− 0.43	±0.10	2.5	J1016−5857	1.20	±0.20	0.64	J1047−6709	0.227	±0.063	2.2
J1048−5832	0.923	±0.049	2.9	J1056−6258	0.152	±0.051	3.1	J1057−5226	0.126	±0.027	1.5
J1114−6100	− 2.18	±0.10	1.4	J1123−6102	0.274	±0.092	0.63	J1239−6832	0.46	±0.12	1.7
J1326−6700	0.348	±0.073	4.4	J1338−6204	0.247	±0.082	1.3	J1452−6036	− 1.39	±0.40	0.54
J1507−4352	0.198	±0.058	2.6	J1543−0620	0.170	±0.050	2.2	J1602−5100	0.442	±0.050	3.8
J1617−4216	0.48	±0.14	0.82	J1637−4642	1.22	±0.23	0.66	J1646−6831	0.303	±0.099	9.8
J1648−6044	0.39	±0.12	0.90	J1651−4246	0.292	±0.041	4.5	J1703−3241	0.123	±0.034	3.2
J1704−5236	1.18	±0.28	0.18	J1717−5800	0.72	±0.22	0.52	J1723−3659	− 0.441	±0.086	0.64
J1741−0840	0.202	±0.064	9.9	J1743−3153	− 1.53	±0.42	0.83	J1759−2205	− 0.562	±0.066	1.1
J1803−2137	− 0.456	±0.089	1.3	J1808−0813	0.181	±0.061	0.52	J1809−1917	− 0.429	±0.058	0.73
J1809−2109	1.21	±0.40	0.69	J1825−1446	1.82	±0.12	1.2	J1832−0827	− 1.96	±0.11	0.22
J1833−0338	0.310	±0.069	1.7	J1833−0827	− 13.11	±0.88	1.7	J1834−0426	0.110	±0.036	2.1
J1836−1008	− 0.262	±0.087	1.9	J1841−0345	− 0.302	±0.082	0.82	J1852−0118	1.74	±0.27	1.2
J1852−0635	0.161	±0.048	4.6	J1853−0004	1.54	±0.31	3.2	J1856−0526	− 1.01	±0.31	0.43
J1906+0912	3.5	±1.2	0.51	J1908+0909	1.30	±0.43	0.50	J1909+0007	3.34	±0.50	11
J1913−0440	0.149	±0.041	3.0	J1915+1009	0.268	±0.070	5.4	J2037+1942	− 0.69	±0.20	3.4

This paper has been typeset from a TEX/LATEX file prepared by the author.